Geophysical Images of the North Anatolian Fault Zone in the Erzincan Basin, Eastern Turkey, and their Tectonic Implications

Ümit Avşar,[1] Erşan Türkoğlu,[2] Martyn Unsworth,[3] İlyas Çağlar,[1] and Bülent Kaypak[4]

Abstract—The collision between the Arabian and Eurasian plates in eastern Turkey causes the Anatolian block to move westward. The North Anatolian Fault (NAF) is a major strike-slip fault that forms the northern boundary of the Anatolian block, and the Erzincan Basin is the largest sedimentary basin on the NAF. In the last century, two large earthquakes have ruptured the NAF within the Erzincan Basin and caused major damage ($M_s = 8.0$ in 1939 and $M_s = 6.8$ in 1992). The seismic hazard in Erzincan from future earthquakes on the NAF is significant because the unconsolidated sedimentary basin can amplify the ground motion during an earthquake. The amount of amplification depends on the thickness and geometry of the basin. Geophysical constraints can be used to image basin depth and predict the amount of seismic amplification. In this study, the basin geometry and fault zone structure were investigated using broadband magnetotelluric (MT) data collected on two profiles crossing the Erzincan Basin. A total of 24 broadband MT stations were acquired with 1–2 km spacing in 2005. Inversion of the MT data with 1D, 2D and 3D algorithms showed that the maximum thickness of the unconsolidated sediments is ∼3 km in the Erzincan Basin. The MT resistivity models show that the northern flanks of the basin have a steeper dip than the southern flanks, and the basin deepens towards the east where it has a depth of 3.5 km. The MT models also show that the structure of the NAF may vary from east to west along the Erzincan Basin.

Key words: Magnetotellurics, electrical resistivity, fault zone conductor, Erzincan Basin, Eastern Turkey.

1. Introduction

The North Anatolian Fault (NAF) is a major strike-slip fault, extending from Karliova in the east

[1] Department of Geophysical Engineering, Faculty of Mines, Istanbul Technical University, Maslak, 34469 Istanbul, Turkey. E-mail: avsaru@itu.edu.tr
[2] Quantec Geoscience, North York, ON, Canada.
[3] Department of Physics, University of Alberta, Edmonton, AB T6G 2G7, Canada.
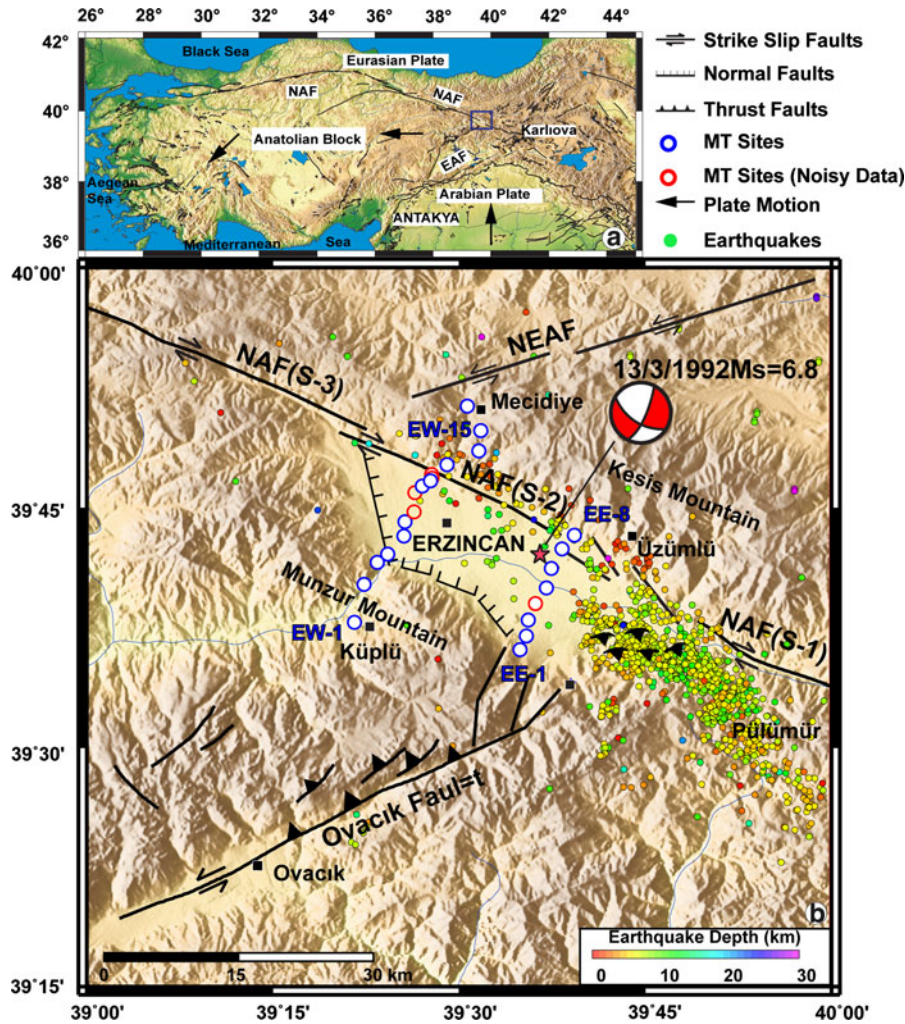[4] Department of Geophysical Engineering, Faculty of Engineering, Ankara University, Ankara, Turkey.

to the Aegean Sea in the west (Fig. 1a). The NAF forms the northern boundary of the Anatolian block, which is moving westward as a result of the collision between the Eurasian and Arabian plates (McKenzie, 1972; Şengör, 1979; Dewey and Şengör, 1979). Recent geodetic measurements suggest that about 70 % of the Arabian-Eurasian plate convergence is accommodated by the westward extrusion of the Anatolian block (Reilinger, 2006) with the slip rate on the NAF estimated from GPS data at approximately 24 mm/year (McClusky et al., 2000).

A series of westward-propagating earthquakes have ruptured the NAF over the last century (Stein and Barka, 1997), and a significant number of earthquakes have occurred in and around the Erzincan Basin over the last millennium (Barka et al., 1987). Severe damage occurred in the city of Erzincan (Fig. 1b) in both the 1939 ($M_s = 8$) and 1992 ($M_s = 6.8$) earthquakes (Barka and Kandisky-Cade, 1988; Fuenzalida et al., 1997). The 1992 event claimed 541 lives (Barka and Eyidoğan, 1993) and had a peak ground acceleration of 0.5 g, and the Mercalli intensity was estimated as IX (Erdik et al., 1992; Gündoğdu et al., 1992).

The analysis of Bayrak et al. (2005) suggested that earthquakes up to magnitude 7.5 could be expected in the Erzincan Basin, and Hartleb et al. (2006) estimated the earthquake recurrence interval as 210–700 years from paleoseismic studies. Although the city of Erzincan has been rebuilt, the seismic hazard remains high because of the high slip rate on the NAF and the fact that the sedimentary basin can significantly amplify ground motion. The strength of ground motion depends primarily on the thickness of sediments in the basin, with the largest amplification occurring in the deepest parts of the

Figure 1

a Topographic map showing the major fault systems of Anatolia; *arrows* show the directions of block motion relative to Eurasia. The *rectangle* indicates the study area. **b** Fault systems in the study area are taken from BARKA and GÜLEN (1989); FUENZALIDA *et al.* (1997) and AKTAR *et al.* (2004). The *dots* indicate the earthquake epicentres from 1960 to 2009 (Kandilli Observatory and Earthquake Research Institute and KAYPAK and EYIDOĞAN, 2005). The focal mechanism solution is from BERNARD *et al.* (1992)

basin and at the edges (OLSEN *et al.*, 1995; OLSEN, 2000). Therefore, the thickness and shape of the sedimentary basin are important parameters to predict the amplification of the ground motion. Furthermore, the depth of the basin is an important parameter for improving 3D earthquake relocation (AKTAR *et al.*, 2004). Several seismic tomography experiments have attempted to map the thickness of the Erzincan Basin. Some of these studies used the 1992 aftershocks and reported the thickness of unconsolidated sediments as 2–4 km. They determined that the boundary between

the upper sedimentary layer and basement was at a depth of 6–12 km. (AKTAR *et al.*, 2004; GÖKALP, 2007; KAYPAK, 2008).

The magnetotelluric (MT) method involves the measurement of the time variations of the orthogonal components of natural electric and magnetic fields, which contain information about the electrical resistivity structure from crustal to upper mantle depths. Magnetotellurics is well suited to image the presence of fluids within the fault zones as well as the thickness and the shape of the sedimentary basin (BOERNER

et al., 1995; Pomposiello *et al.*, 2002; Padilha and Vitorello, 2002).

Seismic and magnetotelluric methods provide images of acoustic velocity (V_p and V_s) and electrical resistivity (ρ) respectively on similar spatial scales (Bedrosian *et al.*, 2007). Thus, joint interpretations of resistivity and seismic velocity can be used in studies where both parameters are controlled by the same lithological parameters (Marquis and Hyndman, 1992; Jones, 1987, 1998; Unsworth *et al.*, 2005). The main factor controlling the elastic and electrical properties of solid–liquid rock mixtures is the amount of liquid present, i.e., the porosity. The clay content and pore geometry can also influence the resistivity (Kozlovskaya and Hjelt, 2000). Because of this fact, unconsolidated sedimentary basins and fault zones can have correlated low seismic velocity and high electric conductivity anomalies.

The purpose of this study is to use MT data to image the geometry of the Erzincan Basin and associated faults. The resulting models are used to evaluate the regional tectonics and seismic hazards in the Erzincan area.

2. Geological and Tectonic Setting

2.1. Regional Tectonics of the Erzincan Area

The Erzincan Basin is 15 km wide and 50 km long; it is bounded on the northern side by the right lateral North Anatolian Fault (NAF). In this region, the NAF has been divided into a number of segments. From east to west these are labelled as S-1, S-2 and S-3 in Fig. 1b (Barka and Gülen, 1989).

- Segment S-1 has a strike direction of N110°E and is located east of the Erzincan Basin.
- Segment S-2 has almost the same strike direction as S-1, forms the northern boundary of the Erzincan Basin and consists of a series of sub-parallel faults with an average strike direction of N133°E (Barka and Gülen, 1989; Aktar *et al.*, 2004). The 13 March 1992 earthquake ruptured this segment (Grosser *et al.*, 1998; Bernard *et al.*, 1992; Fuenzalida *et al.*, 1997).
- Segment S-3 strikes N105°E and extends westward about 110 km. The 1939 Erzincan earthquake

ruptured both segments S-2 and S-3 (Ambraseys, 1970; Barka and Gülen, 1989).

Two left-lateral strike-slip faults, the Ovacık Fault (OF) and the North East Anatolian Fault (NEAF), intersect the NAF at the southern and northern edge of the Erzincan Basin, respectively, (Fig. 1b). The NE-SW trending Ovacik Fault (Arpat and Saroğlu, 1975) or Malatya-Ovacık Fault Zone (Westaway and Arger, 2001) has been interpreted as being inactive at present. It has been suggested that the OF formed the Africa-Turkey plate boundary between 5 and 3 Ma, and became inactive when the left lateral strike slip East Anatolian Fault (EAF) developed east of the OF 3 Ma ago. Since the EAF became the location of motion between the Anatolia and Arabian plates (Fig. 1a) (Over *et al.*, 2004c), the OF has not moved significantly (Westaway and Arger, 2001). However, Grosser *et al.* (1998) indicated that the fault cuts the Quaternary basin fill in the Ovacık Basin and classified it as an active fault. The NEAF (Tatar, 1978) has a NE-SW trend and defines the northern boundary of the part of Eastern Anatolia that is escaping eastward towards the Caucasus (Barka and Gülen, 1989).

The tectonic evolution of the Erzincan Basin is not fully understood. The basin was initially described as a pull-apart basin (Allen, 1969; Aydın and Nur, 1982; Hempton and Dunne, 1984). However, Barka and Gülen (1989) proposed a revised model that suggested that the NAF contributes to the growth of the basin in length, while the OF has increased the width and depth of the Basin (Şengör *et al.*, 2005).

The Erzincan Basin continues to grow in an ENE-WSW direction because of motion on the NAF and OF. The OF splays into several small segments at its northernmost end, and active normal faulting has been mapped along the southern and western margins of the Erzincan Basin (Fuenzalida *et al.*, 1997). Several dacitic-rhyolitic volcanic cones with ages between 0.1 and 1.06 Ma are found on both the northern and southern margins of the basin (Hempton and Dunne, 1984; Karslı *et al.*, 2008). Although the Erzincan Basin lies within the regionally thickened crust of eastern Anatolia, high rates of extension have caused thinning of the crust in the Erzincan area
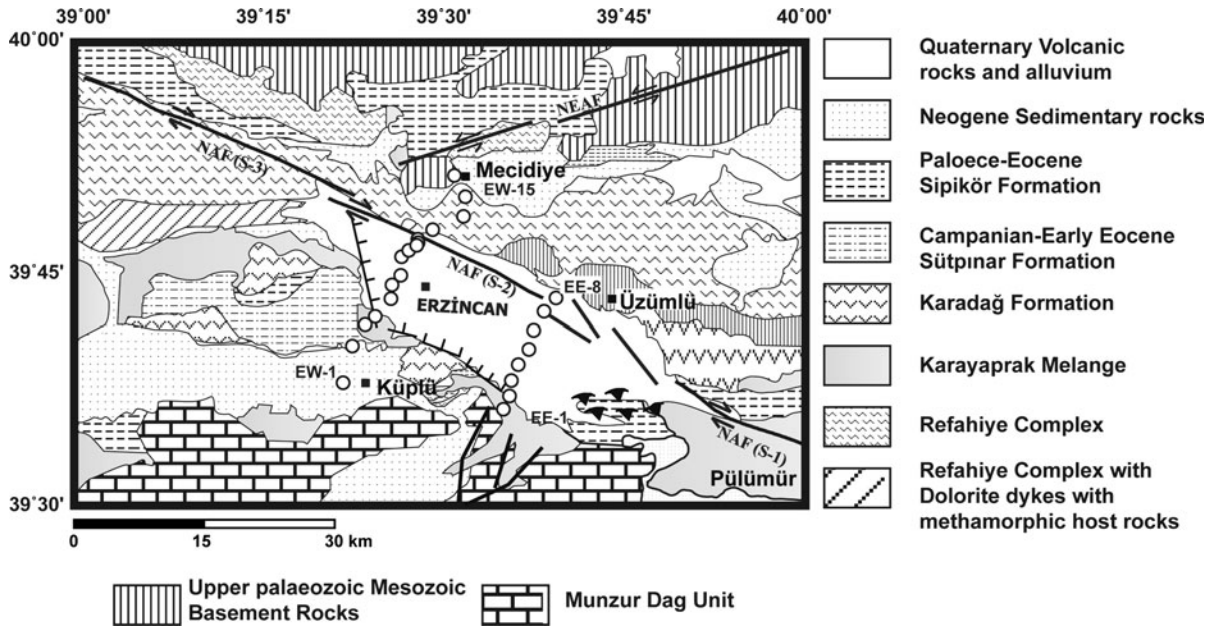
Figure 2
Geological map of the study area modified from RICE *et al.* (2009). The fault structures are the same as in Fig. 1. The *circles* show the magnetotelluric measurement sites

(AYDIN and NUR, 1982; FUENZALIDA *et al.*, 1997; GROSSER *et al.*, 1998; KOÇYIĞIT, 2003).

2.2. Regional Geology

The geological structure of the Erzincan region is complex (Fig. 1) because of a long history of plate interactions and associated deformation. The Erzincan Basin is bounded by the Kesis Mountains in the north and by the Munzur Mountains in the south. These ranges have very different geological structures. The Kesis Mountains are characterised by the Refahiye Complex (Fig. 2), which contains ophiolites with large amounts of serpentinite and metamorphic rocks. The Refahiye Complex is overlain by the Sipikör Formation, which contains siliciclastic and carbonate sedimentary rocks (RICE *et al.*, 2009).

South of the Erzincan Basin, the basement rocks consist of Upper Triassic to Lower Cretaceous carbonates of the Munzur Formation (ÖZGÜL and TURŞUCU, 1984), which was called the Munzur Dag unit by RICE *et al.* (2009). The Karayaprak Melange is a 4-km-thick, variably tectonized mixture of blocks consisting of serpentine, basalt, radiolarite, massive

limestone and volcaniclastic sedimentary rocks. The Sütpınar Formation consists of a 1,500-m-thick, upward-coarsening succession of mixed carbonate siliciclastic sedimentary rocks and subordinate volcanogenic rocks.

The basement rocks on both sides of the basin are covered by Miocene deposits that outcrop extensively west and north of the Erzincan Basin and include limestone, marls, green clay, evaporites and fluvial deposits (TÜYSÜZ, 1993; WESTAWAY and ARGER, 2001; KOÇYIĞIT, 2003; RICE *et al.*, 2009) (Fig. 2).

2.2.1 Geological Structure of the Erzincan Basin

The Erzincan Basin is filled with unconsolidated Plio-Quaternary sediments that contain playa deposits, clastics and basin margin conglomerates. The conglomerates are composed of ophiolitic melange clastics and carbonates. The central part of the basin is filled mostly by silts, sands and gravels (BARKA and GÜLEN, 1989). The thickness of the sedimentary layers has been debated in various papers. The basin depth was estimated by an empirical relation between the length and the thickness of the basin as 2.5–3 km

(HEMPTON and DUNNE, 1984). GAUCHER (1994) esti-
mated the basin depth in the southeastern part of the
basin to be between 0.65 and 2.1 km by using the
SP-converted phase of the aftershocks of the 1992
Erzincan earthquake. AKTAR *et al.* (2004) used the
same aftershocks and modelled the Erzincan Basin
with a depth of 9 km. They imaged a low-velocity
corridor that extended in a NW–SE direction. They
also determined the thickness of unconsolidated
sedimentary units in the basin to be between 3 and
4 km. Following this research, a 1D crustal velocity
model was derived for the Erzincan Basin for both P
wave and S wave velocities, and the thickness of
unconsolidated sediments in the basin was estimated
as 2 km (KAYPAK and EYIDOĞAN, 2005). After 1D
interpretation of the seismic velocity structure of the
basin, KAYPAK (2008) derived a 3D V_p and V_p/V_s
velocity model and estimated the unconsolidated
basin depth to be in the range of 2–3 km. Recently,
GÜRBÜZ (2010) studied the geometry of the Erzincan
Basin and estimated the basin depth as ∼4 km.

The electrical resistivity of unconsolidated sedi-
ments is much lower than that of crystalline basement
rocks. The resistivity of sediments is sensitive to
variations in porosity. This allows geophysical tech-
niques such as magnetotellurics to estimate the
thickness of a sediment layer and to map subsurface
porosity. In the following sections, magnetotelluric
data collected in the Erzincan Basin are described and
interpreted.

3. Magnetotelluric Data Collection

The Erzincan magnetotelluric (MT) data descri-
bed in this paper were collected as part of the Eastern
Anatolian Magnetotelluric Experiment in 2005
(TÜRKOĞLU, 2009). Since the Erzincan Basin and NAF
are oriented approximately NW–SE, MT soundings
were collected at 24 sites on two profiles that were
normal to the NAF with a nominal site spacing of
1–2 km (Fig. 1b). The MT data were recorded with
Phoenix Geophysics V5-2000 magnetotelluric sys-
tems. The instruments were synchronised with timing
signals from global positioning satellites (GPS) to
permit remote reference time series processing
(GAMBLE *et al.*, 1979). MT data at most stations were

of acceptable quality; one station on the East Profile
(EE4) and four stations on the West Profile (EW7,
EW8 EW11 EW12) could not be used because of the
high levels of cultural noise around the city of
Erzincan (Fig. 1b). The MT impedance tensor
(Z) and vertical magnetic field transfer functions
(T) were calculated using the statistically robust
method of EGBERT and BOOKER (1986).

4. Dimensionality Analysis and Directionality

Before MT data can be interpreted, dimensional-
ity analysis is needed to determine if a 1D, 2D or 3D
analysis is required. A range of dimensionality anal-
ysis techniques was applied to the Erzincan data, as
described below. If the data can be shown to be
approximately 2D, then a key part of the analysis is to
determine the strike direction.

4.1. Tensor Decomposition

Estimation of the geoelectric strike can be com-
plicated by small, near-surface conductivity
heterogeneities that alter the direction and amplitude
of the measured electric fields. These distortions are
generally frequency independent and referred to as
galvanic distortions (GROOM and BAILEY, 1989; BAHR,
1988). There have been various decomposition
approaches to remove these distortions and determine
the geoelectric strike direction. One of the most
widely used approaches is the Groom and Bailey
(GB) tensor decomposition. In this method the
distortion is assumed to be due to local three-
dimensional (3D) conductivity structures, whereas
the regional conductivity structure is assumed to be
2D.

Tensor decomposition was applied to the Erzincan
MT data with the algorithm of MCNEICE and JONES
(2001), which is an extended form of the GB
decomposition that can consider multiple MT stations
and multiple frequencies. The period-dependent
strike direction was computed for both profiles, as
shown in the first column of Fig. 3. The dominant
strike direction at short periods (0.001–0.1 s) is
between N125°–135E°, which is consistent with the
strike direction of the surface trace of the NAF in the

basin. This gradually changes to N60°–70°E at longer periods (1–1,000 s) that penetrate to lower crustal depths. The latter seems to be the regional strike direction of the area as also reported by TÜRKOGLU et al. (2008). Note that there is an inherent ambiguity of 90° in these directions, so strike directions orthogonal to those listed above are also consistent with the data. The frequency-dependent strike direction indicates that the subsurface resistivity structure is somewhat 3D. Since the focus of this article is on the upper crustal structure corresponding to the basin, the fault parallel strike direction was chosen. This may introduce errors in the deeper parts of a resistivity model, and this can be investigated by analysis of the root-mean-square (r.m.s.) misfit errors computed by the decomposition. This is a quantitative way to evaluate the validity of the tensor decomposition approach as plotted in Fig. 4a. The relatively low r.m.s. misfit values indicate that tensor decomposition is valid for both profiles at periods of less than 10 s (with the exception of stations EW1 and EW2).

4.2. Phase Tensor

Tensor decomposition has the limitation that it makes a number of assumptions about the geoelectric structure in the study area, e.g., the regional geoelectric structure is 2D (BIBBY et al., 2005). CALDWELL et al. (2004) introduced a method that provides a partial solution for the undistorted impedance tensor directly from the observed (distorted) impedance tensor where near-surface heterogeneity and regional conductivity structures are 3D. The method is based on the phase of the impedance tensor, which is not affected by galvanic distortions (CALDWELL et al., 2004; BIBBY et al., 2005). The phase information is defined by the phase tensor $\Phi = \mathbf{X^{-1}} \times \mathbf{Y}$ where $\mathbf{X}$ and $\mathbf{Y}$ are the real and imaginary parts of the impedance tensor. The non-symmetric phase tensor can be represented graphically as an ellipse, defined by the major axis Φ_{max}, the minor axis Φ_{min} and the skew angle β. The parameter α expresses the tensor dependence on the chosen coordinate frame. If the conductivity distribution is 1D, then the phase tensor will be a unit circle and the skew angle $\beta = 0$. In the 2D case, $\beta = 0$ and α is the direction parallel or

normal to the regional strike direction. However, in a 3D situation the skew angle β will be non-zero, and induced electric currents will flow in the direction of the major axis $(\alpha–\beta)$.

The phase tensor method was applied to the Erzincan MT data, and the results are shown in the second column of Figs. 3 and 4b. The $\alpha–\beta$ direction was found to be between N90-120°E at short period bands (0.001–10 s) and N40–50°E at long period (10–1,000 s). These strike directions for long periods are consistent with the other approaches described in Sect. 4.1. However, there are some differences in the short-period data (0.1–10 s); these could be distortions related to the complex structure of the Erzincan area.

Figure 4b shows a pseudo section of the phase tensor ellipses for the two profiles as a function of period. The colour of the ellipses shows the value of the skew angle β. According to the figure, high β values are observed at periods greater than 1 s. Thus, it perhaps can be concluded that 3D effects are present in the measured impedances at these periods.

4.3. Induction Vectors

MT strike directions computed with the methods described above contain an inherent 90° ambiguity. This ambiguity can be removed by reference to geological information or by using the vertical magnetic field, provided the structure is isotropic. The magnetic field transfer function $T = [T_x, T_y]$ relates the vertical and horizontal magnetic fields through $H_z = T_x H_x + T_y H_y$. This function can be graphically represented by plotting as an induction vector. The real induction vector has components $[\text{Re}(T_x), \text{Re}(T_y)]$ (PARKINSON, 1962; WIESE, 1962) and is widely used for dimensionality and directionality analysis. The real induction vector points at conductive discontinuities when plotted in the Parkinson convention. In an ideal 2D geometry, the induction vectors will be perpendicular to the geoelectric strike direction and provide a way to overcome the inherent ambiguity in strike directions estimated from the impedance tensor. Induction vectors for the Erzincan data are plotted in the Parkinson convention in Fig. 5. The directions of the induction vectors show significant scatter and are
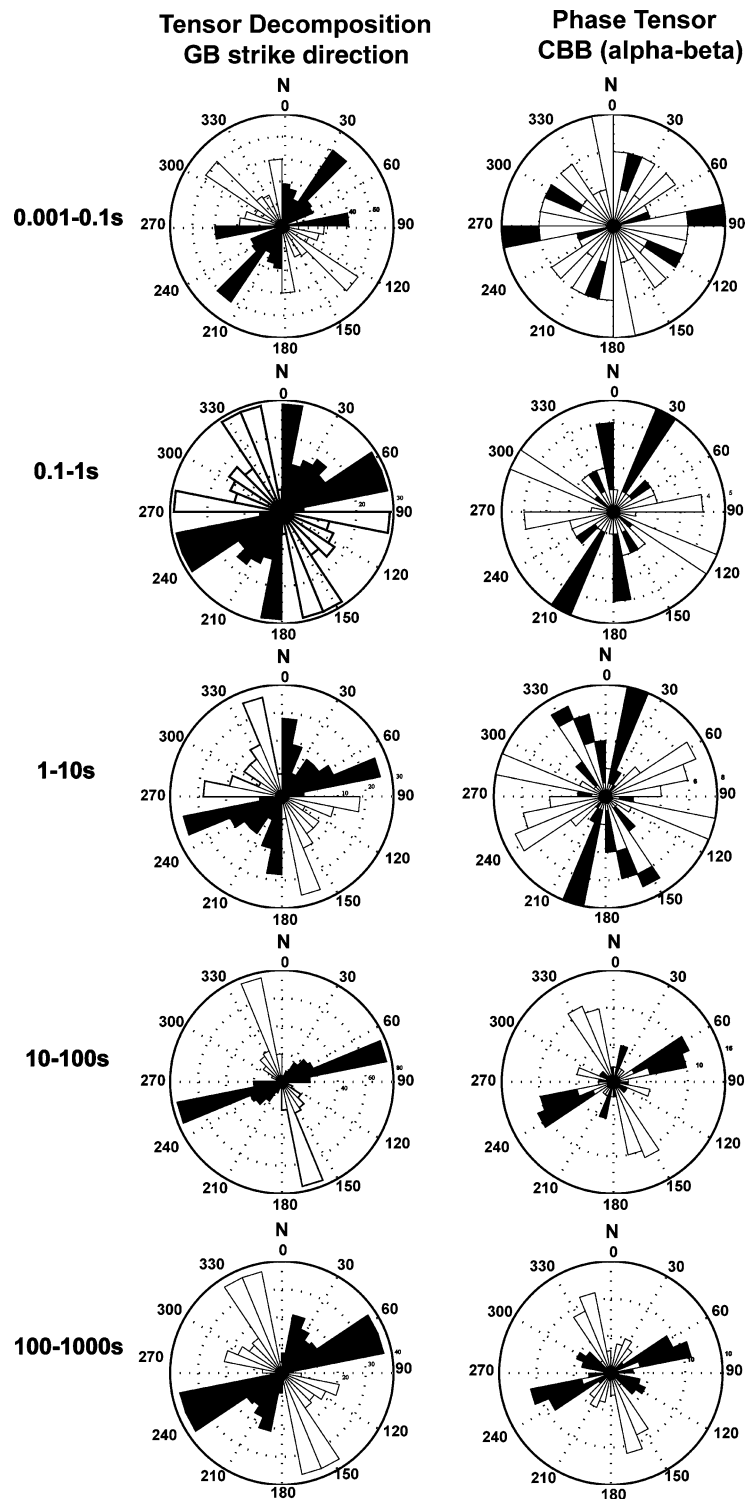
Figure 3
Geoelectric strike directions obtained for five period bands. *Black and white histograms* represent the 90° ambiguity in the MT geoelectric strike direction. The co-centred circles (*dashed*) indicate the total number of the frequencies that has the same strike angles in chosen period bands at all stations. *GB* Groom Bailey, *MJ* MᴄNᴇɪᴄᴇ and Jᴏɴᴇꜱ (2001), *CBB* Cᴀʟᴅᴡᴇʟʟ *et al.* (2004)
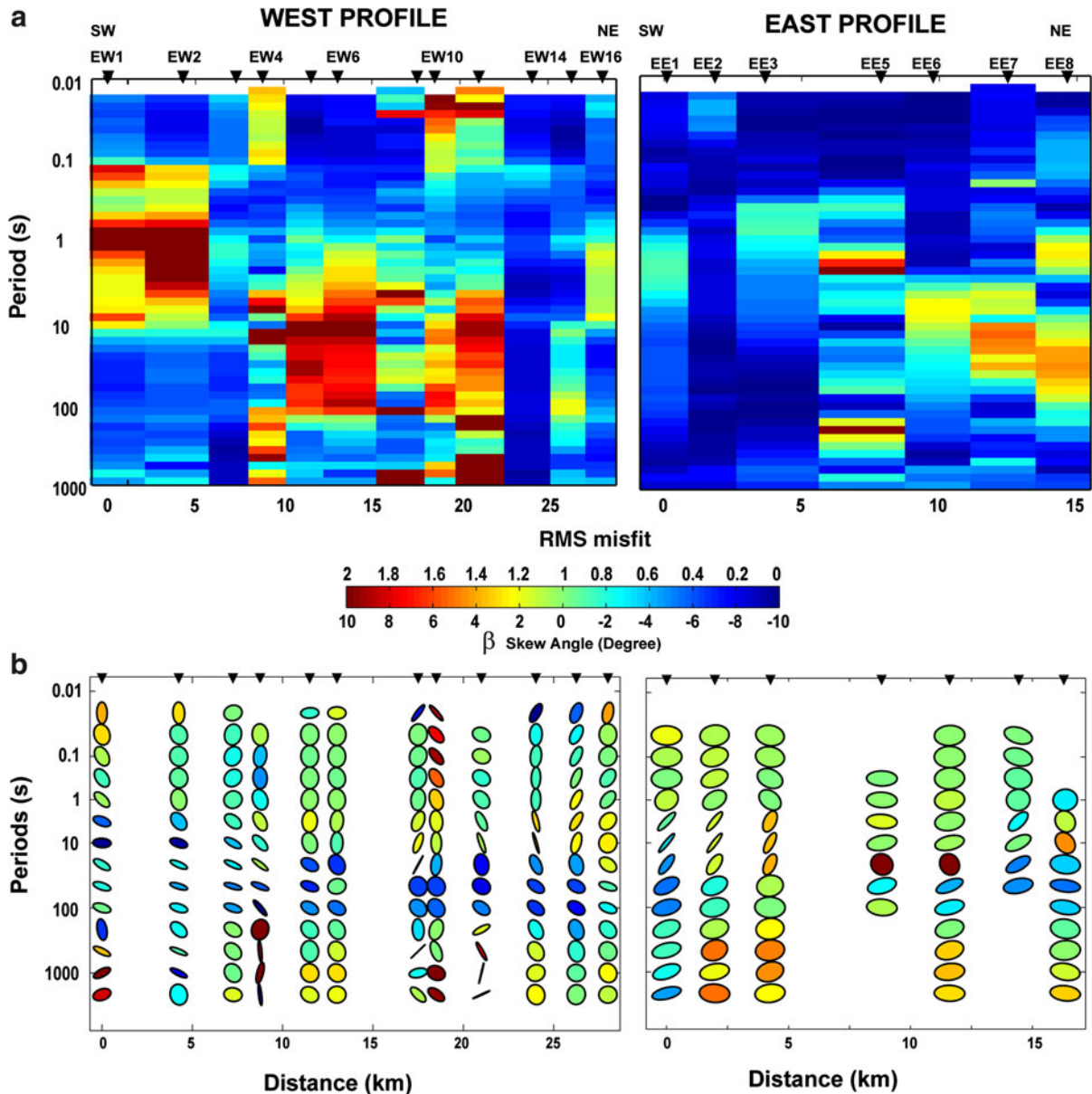
Figure 4
a The RMS misfit of tensor decomposition for the whole period band. **b** Phase tensor ellipses at two profiles. The *colour* of the ellipses indicates the skew β

inconsistent with an ideal 2D scenario. This scatter could be due to either noise in the data or a 3D geoelectric structure. Short induction vectors in the middle of the basin may indicate a 1D geoelectric structure. Stations at the edge of the Erzincan Basin have longer induction vectors, indicating a strong horizontal change in conductivity. These induction vector directions suggest that the geoelectric structure

of the region is 3D rather than 2D, consistent with the complex pattern of faults shown in Fig. 1b.

In summary, MT data indicate a complex 3D geometry for the Erzincan Basin, and a 2D analysis of these data should be undertaken with care. Overall, the geoelectric strike direction of the Erzincan Basin is about N120°E at short periods (0.001–10 s) and is consistent with the strike direction of the surface trace of
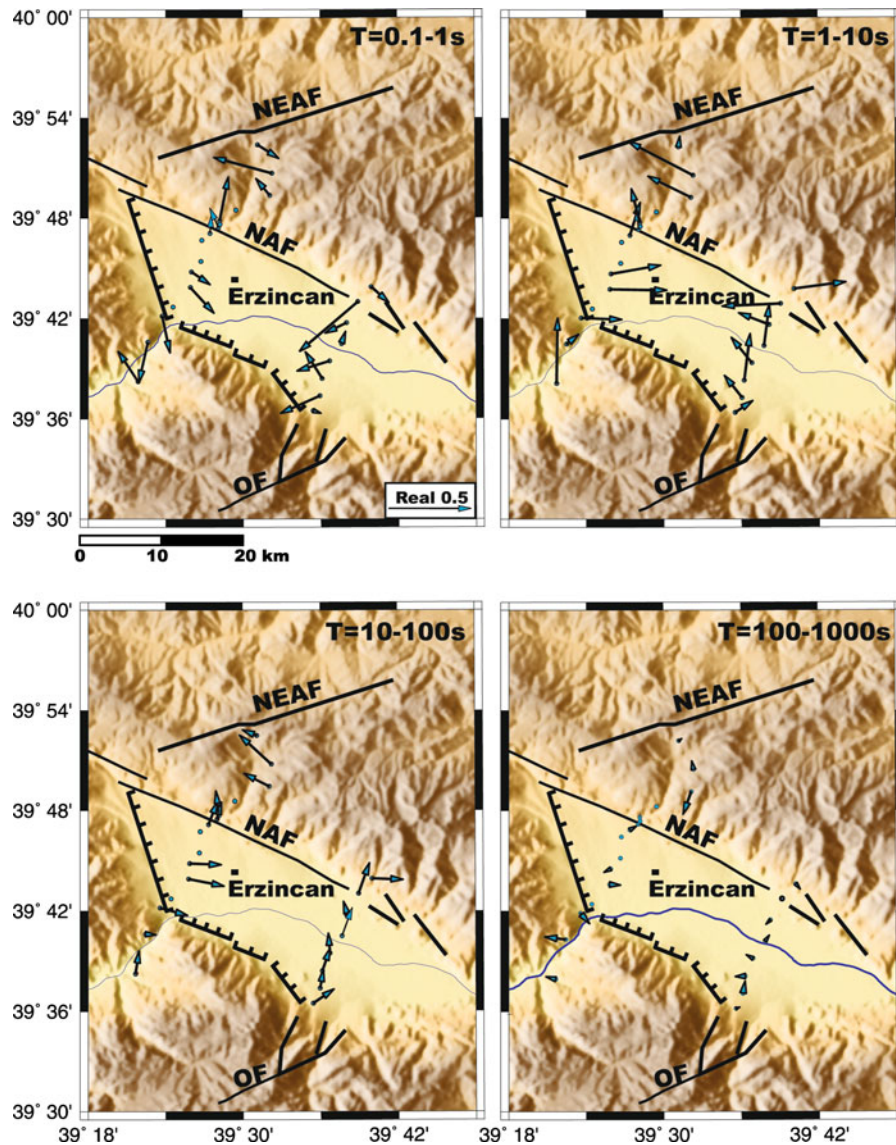
Figure 5
Real induction vectors for different period bands plotted in the Parkinson convention

the NAF (BARKA and GÜLEN, 1989; AKTAR et al., 2004). The geological constraint was essential in overcoming the 90° ambiguity, owing to the scatter in the induction vectors. At longer periods the strike direction is between N60°–70°E in the Erzincan region.

5. Magnetotelluric Modeling of the Erzincan Basin

Magnetotelluric data are recorded in the time domain and transformed to the frequency domain for analysis, with the lowest frequencies sampling deepest into the Earth. To obtain a resistivity model as a function of true depth, forward modelling or inversion methods need to be applied to the MT data. The Erzincan MT data have been analysed with 1D, 2D and 3D approaches, as described in the following sections.

5.1. Magnetotelluric Data

The impedance tensor was rotated in the co-ordinate system of N120°E that was derived in Sect.

4, and apparent resistivity and phases were computed. The vertical magnetic field transfer function was also projected into this co-ordinate system. Figures 6 and 7 illustrate the apparent resistivity, phase and vertical magnetic field transfer function data in pseudosection format and fitting curves format, respectively. Three main features can be observed in the data:

- Nearly constant phase values are observed over the period range 0.01–1 s for both polarizations of the MT impedance data. This implies that the shallow resistivity structure does not vary strongly vertically or horizontally in the Erzincan Basin.
- Increasing apparent resistivity in the period range 1–30 s.
- Decreasing apparent resistivity at periods longer than 30 s. This implies the presence of a low resistivity (conductive) layer at depth.

5.2. One-Dimensional (1D) Inversion of the Erzincan MT Data

One-dimensional inversion was performed using WinGlink[1] software package, which allows the user to fix the resistivity or thickness of a layer. MT stations inside the Erzincan Basin where the apparent resistivity and phase curves suggest a 1D geoelectric structure (Fig. 7 and Supplementary FigA2) were used in 1D inversion to estimate the basin thickness. Since the boundary between the low resistivity basin sediments and the upper crustal crystalline rocks is expected to be sharp, this approach is useful because it permits sharp changes in the resistivity. MT data from four stations were inverted using this approach. Two stations were chosen from the central West Profile (EW-5 and EW-6), and the other two stations were chosen from the central East Profile (EE-5 and EE-6). Initial inversions revealed a three-layer resistivity structure with the middle layer having a higher resistivity than those above and below. The upper conductive layer can be identified as the sedimentary basin. The estimated thickness of the basin was observed to vary significantly between closely spaced

---

[1] WinGLink is a multidisciplinary software program developed by WesternGeco to process, interpret and integrate geophysical data.

MT stations on both profiles. This is primarily due to the presence of static shifts in the MT data. In addition non-uniqueness arises in the MT inverse problem because only the conductance of a buried layer is well defined by MT data. Various combinations of layer conductivity and thickness with the same product will all be able to fit the measured data. Therefore, a thick, lower conductivity layer will give exactly the same MT response as a thin, more conductive layer. However, in this study, the conductive layer is located at the surface, and the non-uniqueness problem is less serious. This is because the highest frequency data directly sample the conductivity of the upper part of the layer, partially overcoming the non-uniqueness.

The seismic velocities in this area are between 4.5 and 5.5 km/s, and according to MEJU et al. (2003) these velocities correspond to 500–900 Ωm resistivities. Thus, in our analysis, the resistivity of the second layer (a resistive layer between two conductors) was fixed to 500 Ωm (Fig. 8 and Supplementary Fig.A1) with the assumption that the resistivity of the basement rock does not change significantly over such short distances. In this case, the 10–30 Ωm top layer that corresponds to the sedimentary fill of the Erzincan Basin has a thickness in the range of 2.9–4 km and 2.5–3.6 km in the West and East, respectively. Thus, the mean thickness of the Erzincan Basin can be estimated as 3.25 ± 0.67 km.

5.3. Two-Dimensional (2D) Inversion of the Erzincan MT Data

In the previous section, it was shown that the Erzincan MT data can be considered 2D in the period band 0.01–100 s with a strike-direction of N120°E. When the earth is assumed to be two-dimensional, the data can be divided into two independent modes: (1) the transverse-electric (TE) mode has electric current flowing parallel to the geoelectric strike direction and (2) the transverse-magnetic (TM) mode with electric current flowing perpendicular to the geoelectric strike direction. These two modes are sensitive to different aspects of the subsurface resistivity structure. The TE mode is particularly sensitive to along-strike conductors, whereas the TM mode is more sensitive to resistive features (WANNAMAKER et al., 1989;
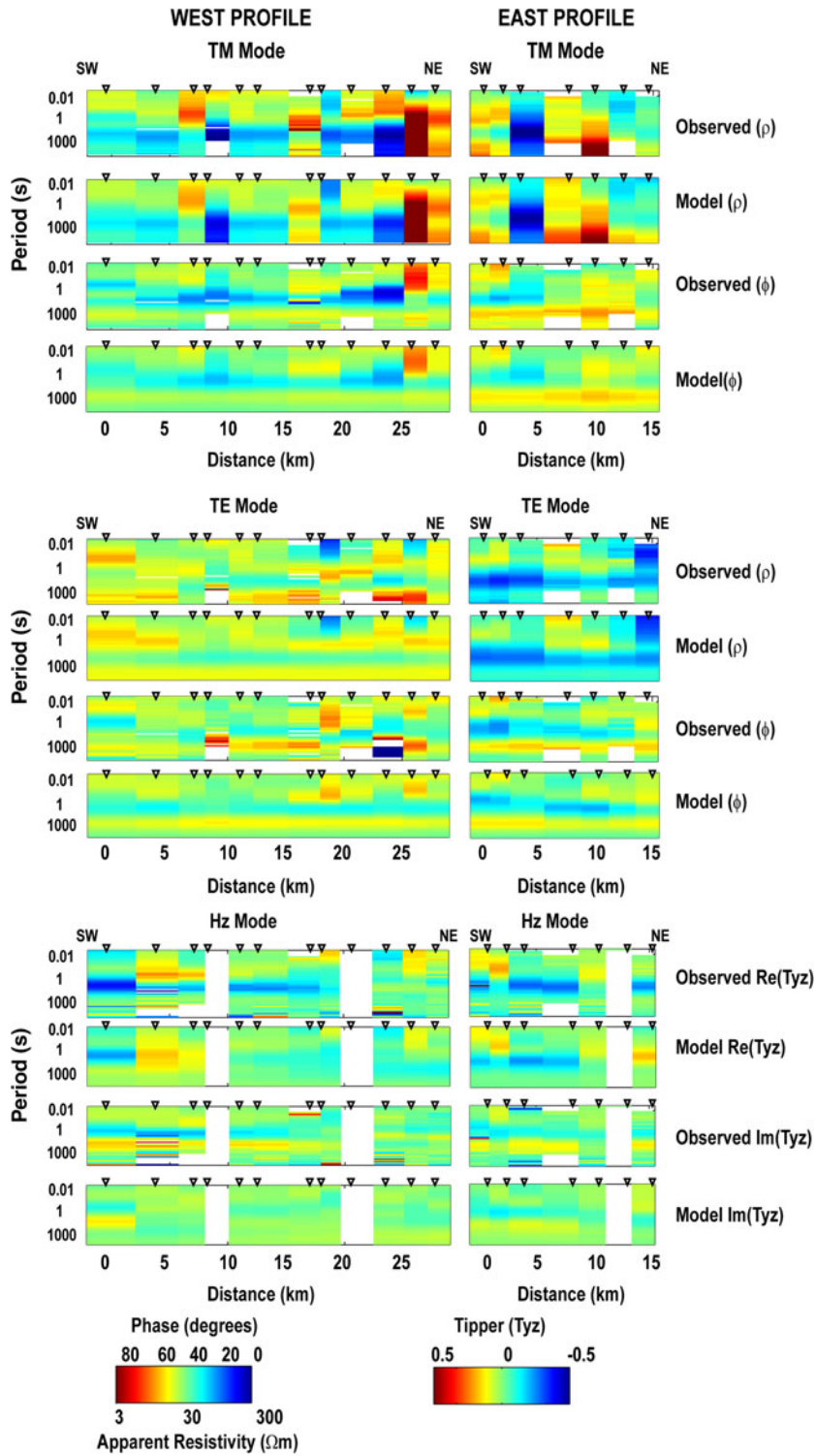
Figure 6
Pseudosections of the observed and modeled apparent resistivity, phase and tipper data for the inversion models shown in Fig. 10 for the West and East Profiles, respectively. Two stations on the West Profile and one station on the East Profile do not have tipper data, since the instruments recording only electric fields were used. At these stations, impedances were computed with magnetic fields from adjacent stations
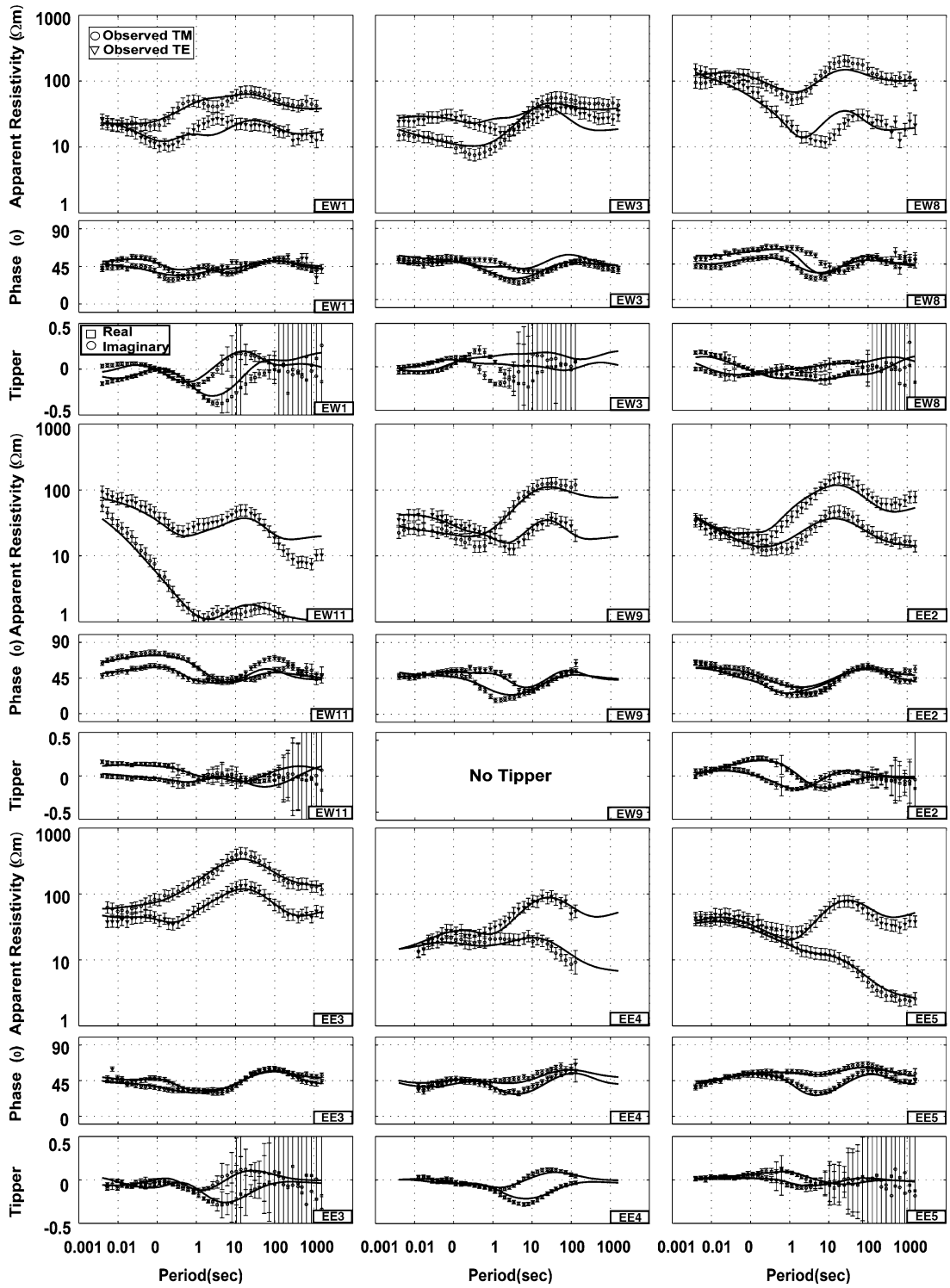
Figure 7
Examples of apparent resistivity, phase and tipper curves after 2D inversion with $\tau = 10$ and $\alpha = 7$. Error floors of 20 and 10 % were applied to the resistivity and phase data, respectively. The error floor for the tipper data was set to 0.02. *Symbols* and *solid lines* indicate the observed data (rotated data) and inversion model responses, respectively. The phases are shown in the first quadrant
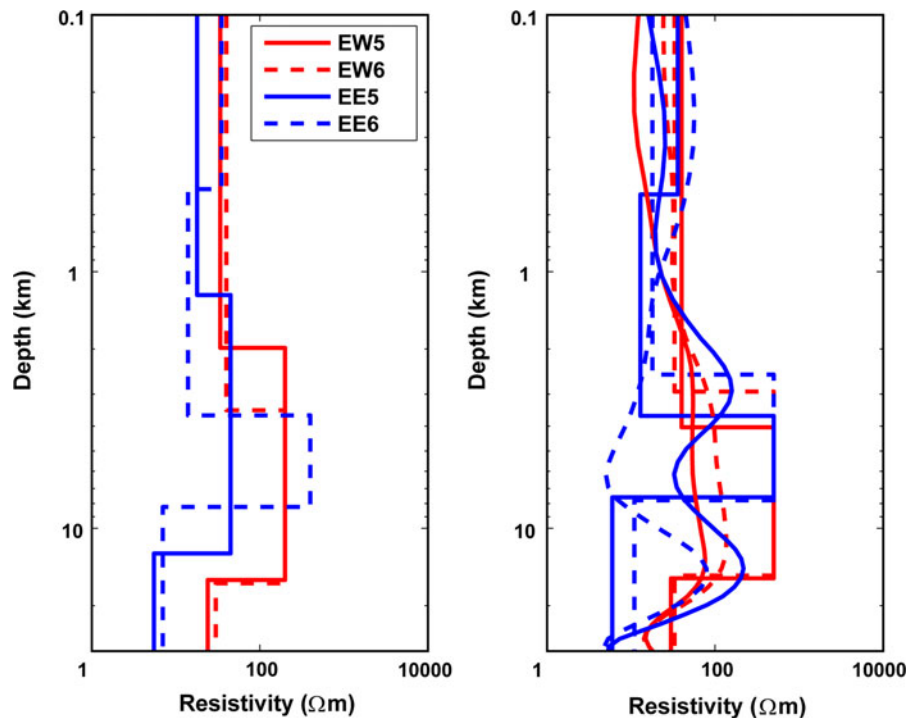
Figure 8
One-dimensional sharp layered inversion for the central stations on the West and East Profiles. The *left panel* shows models obtained by unconstrained 1D inversion. Models in the *right panel* were obtained by fixing the resistivity of the resistive layer to 500 Ωm. *Straight lines* and *curves* are 1D and 2D inversion results, respectively (Türkoğlu, 2009)

BERDICHEVSKY *et al*., 1998). The tipper is part of the TE mode and is sensitive to lateral variations in conductivity. Because the TE and TM modes and the tippers are sensitive to different features, all combinations of these data sets should be inverted if possible to obtain the most comprehensive image of subsurface conductivity. The inversion algorithm (NLCG6) of RODI and MACKIE (2001) was used for the 2D inversions. The magnetotelluric inverse problem is inherently non-unique, which means that a number of models can be found to fit the measured MT data with the same accuracy. This problem can be addressed by regularization of the resistivity models, which requires that additional constraints are imposed on the resistivity model. This is most often implemented by requiring the resistivity model to be spatially smooth (HANSEN, 1992). The NLCG6 algorithm implements a TIKHONOV and ARSENIN (1977) type of regularization method, and seeks the smoothest model with the least deviation from an a priori model. The parameter τ determines the degree of smoothing and controls the trade-off between generating a smooth model and fitting the measured MT data. A high value of τ gives a spatially smooth model at the expense of poor data fit. In contrast, a small value of τ produces a better fit to the data, but the model can be unrealistically rough. Thus, the selection of the optimal regularization parameter τ is important. Another regularization parameter in the NLCG6 algorithm is denoted by α, which controls the balance between horizontal and vertical smoothness of the resistivity model. A value of $\alpha > 1$ produces models with horizontal layering, while a value of $\alpha < 1$ produces vertical structures.

The 2D inversions started from a half-space model with a resistivity of 100 Ωm and included topography. Error floors of 20 %, 10 % and 0.02 were assigned to the apparent resistivity, phase and tipper data, respectively. The static shift coefficients were estimated during the generation of the 2D models and found to be in the range of 0.1–10. The L-curve method was used to determine the appropriate value of τ, which represents a trade-off between model roughness and data misfit. The distinct corner,

separating the vertical and horizontal branches of the L-curve, corresponds to the optimal value of τ (HANSEN, 1992; BOOKER et al., 2004). A range of τ values from 0.7 to 1,000 was investigated, and $\tau = 10$ was chosen as the optimal value (Fig. 9a). The dependence of the final model on α was also investigated (Fig. 9b), which determines if smoothing is dominantly in the horizontal or vertical direction. Because the Erzincan Basin consists of horizontally deposited sedimentary layers, a value of $\alpha = 7$ was used to produce a resistivity model with horizontal layering. After testing many inversions, which included inversions of different combinations of the modes with different τ values (0.7–1,000) and α values (1–20) (Fig. 9), the models obtained by joint inversions of the TE, TM and tipper mode data were accepted as final models for the East and West Profiles (Fig. 10a). The models fit the measured MT data with the statistically acceptable normalized root-mean-square (r.m.s) misfit of 2.82 and 1.17 for the West and East Profiles, respectively. Site-by-site misfit and static shift coefficients are shown in Fig. 10a and indicate an acceptable fit, except for station (EW14) on the West Profile. Inversions were run with station EW14 excluded, and the final resistivity models were similar to those that included this station for $\alpha = 1$, 3 and 5, and the r.m.s misfit was reduced to 1.45. However, when α was larger, the inversion model was different from the model that included station EW14. When station EW14 was not used, the gap between the stations at the NE end of the West Profile became large, and for large α values (smoothing horizontally) the model became insensitive to the geometry of the basin edge. The static shift coefficients are generally in the range 0.1–10 on both profiles, with 1 indicating no shift. Comparison between the observed MT data and calculated responses for the West and East Profiles show the data are well fit, both in pseudosections as well as apparent resistivity and phase curves (Figs. 6,7 and Supplementary Fig. A3).

5.4. Three-Dimensional (3D) Inversion of Erzincan Basin MT Data

The 2D analysis described above can be justified by the success of the 2D inversions. However, there are indications of 3D effects in the Erzincan MT data such as (1) the scattered induction vector directions, and (2) the difference between short and long period strike directions. This suggests that 3D inversions are needed to examine the validity of the 2D inversions. The 3D MT inversions were carried out using the code WSINV3DMT, which uses a variant of the OCCAM minimum structure approach (SIRIPUNVA-RAPORN et al., 2005). This reduces the computer time required compared to a model space approach such as that proposed by MACKIE and MADDEN (1993) and SASAKI (2001).

An homogeneous 100 Ωm starting model was generated with 28 and 50 cells in the x and y directions, respectively, and 45 layers in the vertical direction (Fig. 11a). The full impedance tensor data were inverted at four periods per decade with an error floor of 10 % for off-diagonal elements and 20 % for the diagonal elements. The tipper data were not included in the inversion owing to their noisy character. The final 3D resistivity model was obtained after seven iterations with an r.m.s. misfit of 1.78. The 3D model response curves of the impedance tensor (Z_{xy} and Z_{yx}) together with the observed MT data are shown in Fig. 11b. The fit to all four elements of the impedance tensor is shown in the ESM appendix, figure A4. Figure 10 shows a comparison of the 3D and 2D inversions. Note that the 3D inversion models did not include topography. Two- and three-dimensional inversion results showed consistent model features, but the locations of the most pronounced conductive bodies have some lateral offsets. This could be a consequence of two fundamental assumptions made for 2D inversions: (1) We assumed the subsurface resistivity structure is 2D, and (2) the MT sites are projected onto a straight line perpendicular to the profile rather than being inverted at their original locations as in the 3D inversions.

6. Interpretation

6.1. Erzincan Basin

The 2D model and two co-incident slices of the 3D resistivity model (Fig. 10a, b) display a number of similarities. Note that the depths of the structures are
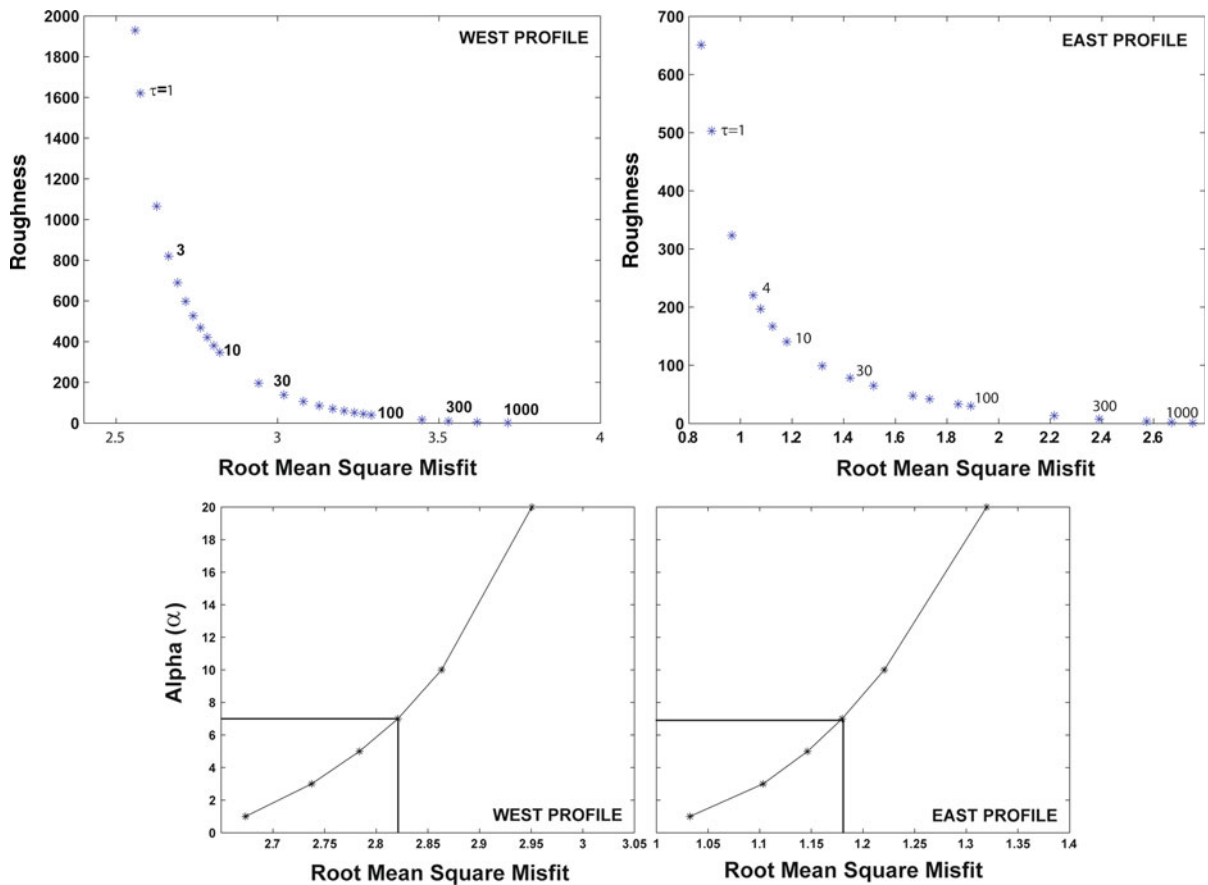
Figure 9
L-curve of the r.m.s misfit as a function of model roughness for different τ (*top*) and α values (*bottom*)

given from the earth surface, not sea level. The most significant feature observed in the 2D inversion models is a conductive region (C1) having the resistivity of 10–30 Ωm and extending to a depth of ∼3 km on both the West and East Profiles (Figs. 10a, 12). Similar features can be observed in the 3D resistivity model, although it should be noted that the grid used in the 3D inversion is coarser than that used in the 2D inversion (Fig. 10b). Because unconsolidated sediments have low electrical resistivities (1–20 Ωm) (KELLER, 1987; PALACKY, 1987), this zone can be interpreted as unconsolidated Quaternary basin sediments. Slightly higher resisitivities of 40–60 Ωm extend to depths of 3–5 km in both of the 2D sections. This zone could be more compacted sediments of the Erzincan Basin at depth.

At the NE end of the West Profile a surface conductor (C3) with a resistivity of 5–30 Ωm is observed. The depth extent of this feature is different in the 2D and 3D inversions (Fig. 10a, b). This conductor could be related to the Sipikör Formation, and Neogene sediments that overlie the Refahiye complex and serpentinite could partially explain the low resistivity (RICE *et al.*, 2009) (Fig. 2). The serpentinite does not create the low resistivity by itself; the cause is rather groundwater that could be naturally present or released from metamorphic reactions (BEDROSIAN *et al.*, 2004). An alternative explanation for the low resistivity is the presence of sedimentary rocks. A similar surface conductor with a resistivity of 5–30 Ωm (C4) is located at the SW end of the West Profile (Fig. 10a, b). This layer represents the Karayaprak Melange, which is a 4-km-thick layer composed of tectonized blocks of serpentinite, basalt, radiolarite, massive limestone and volcaniclastic sedimentary rocks and the Sütpınar Formation, which
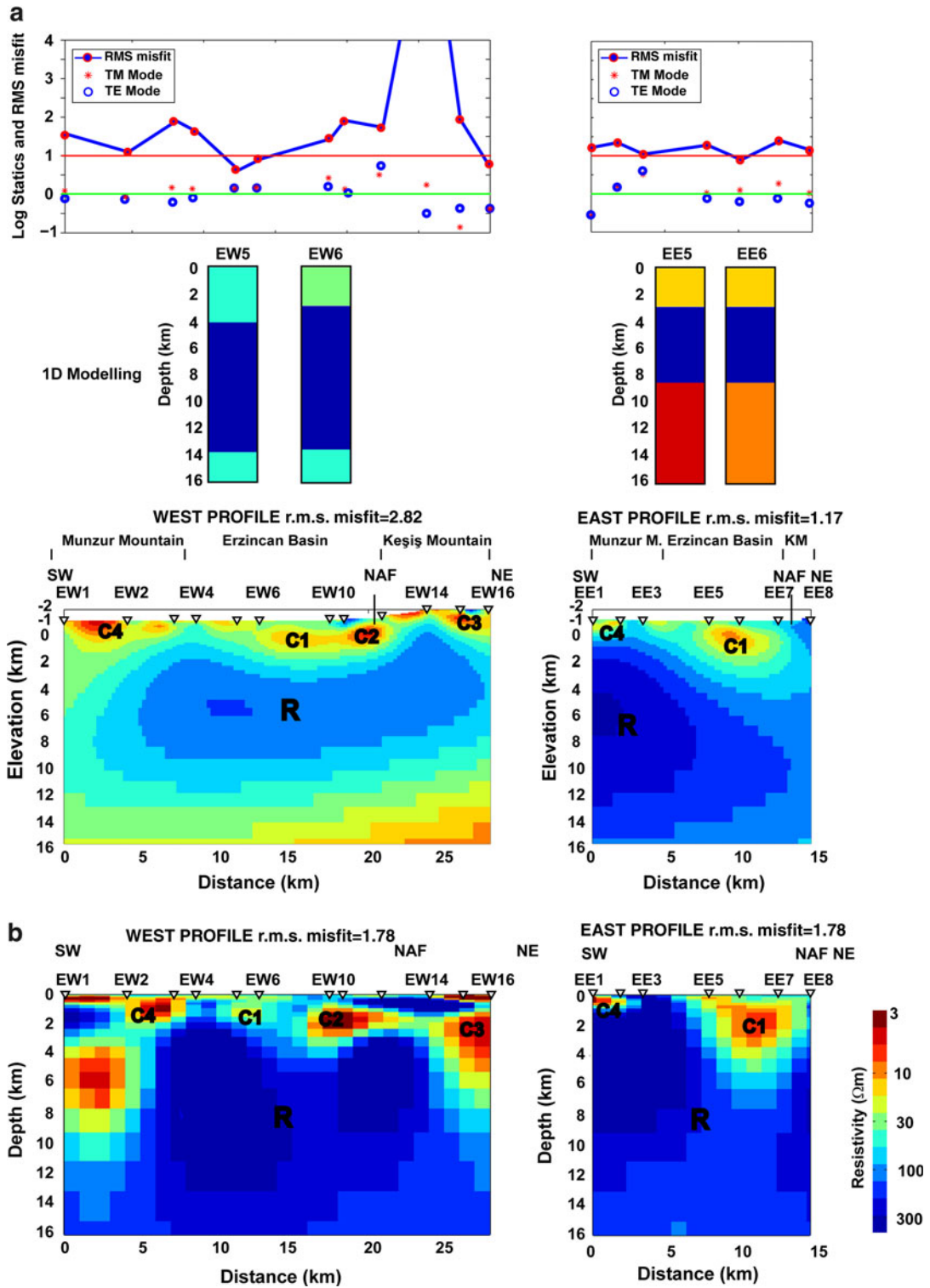
Figure 10
Electrical resistivity models for the West and East Profiles obtained from **a** 1D and 2D inversions of the TE, TM and tipper data; **b** 3D inversion of the full impedance tensor without the tipper data. The r.m.s misfit for individual MT stations is plotted above the 2D models, along with static shift coefficients estimated by the inversion algorithm
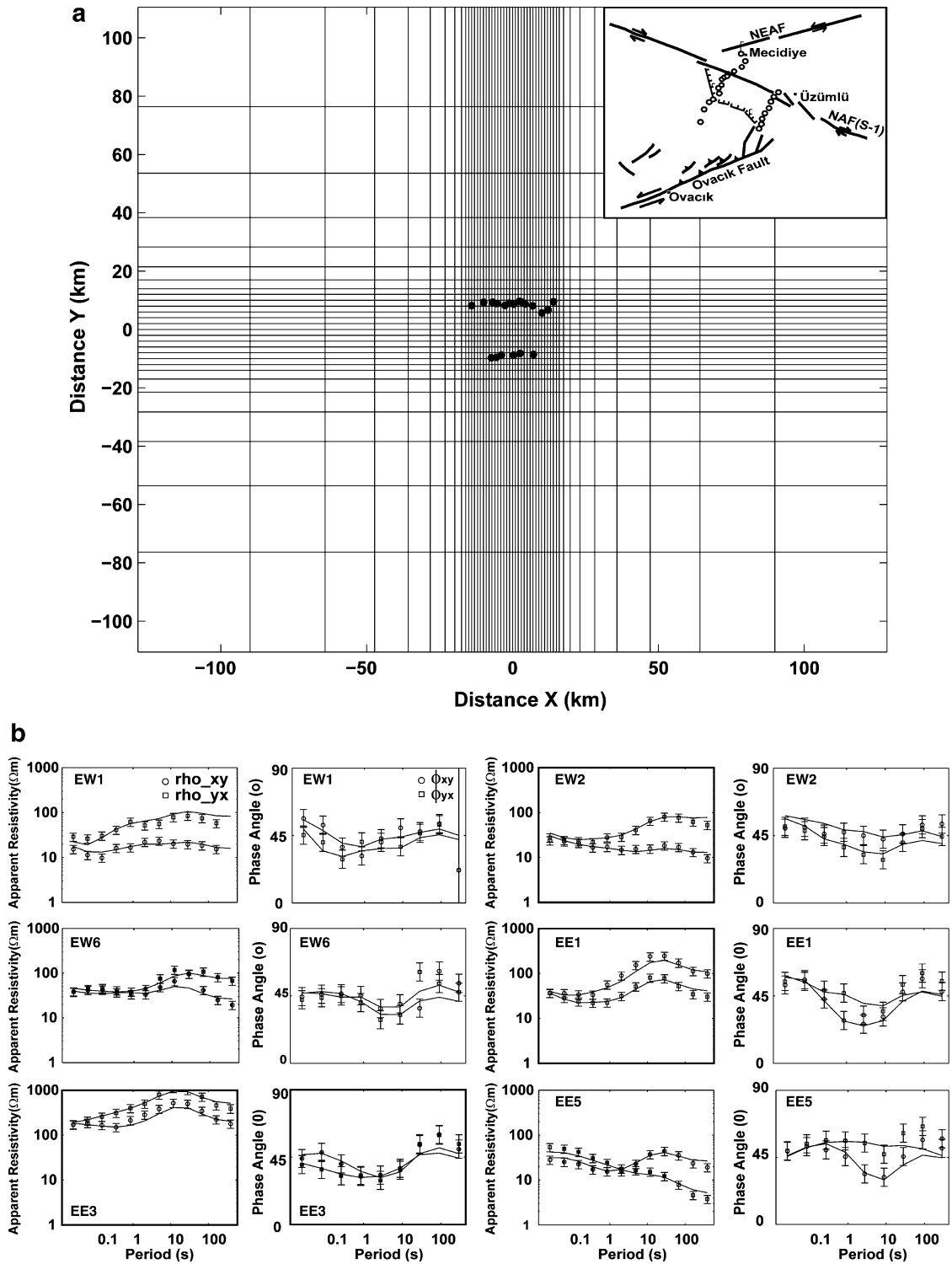
Figure 11

a Mesh structure that was used in 3D modelling and rotated to be parallel to the profiles to reduce computational time. **b** Examples of Z_{xy} and Z_{yx} apparent resistivity and phase curves for some stations in the Erzincan Basin. *Solid lines* illustrate responses from 3D inversion
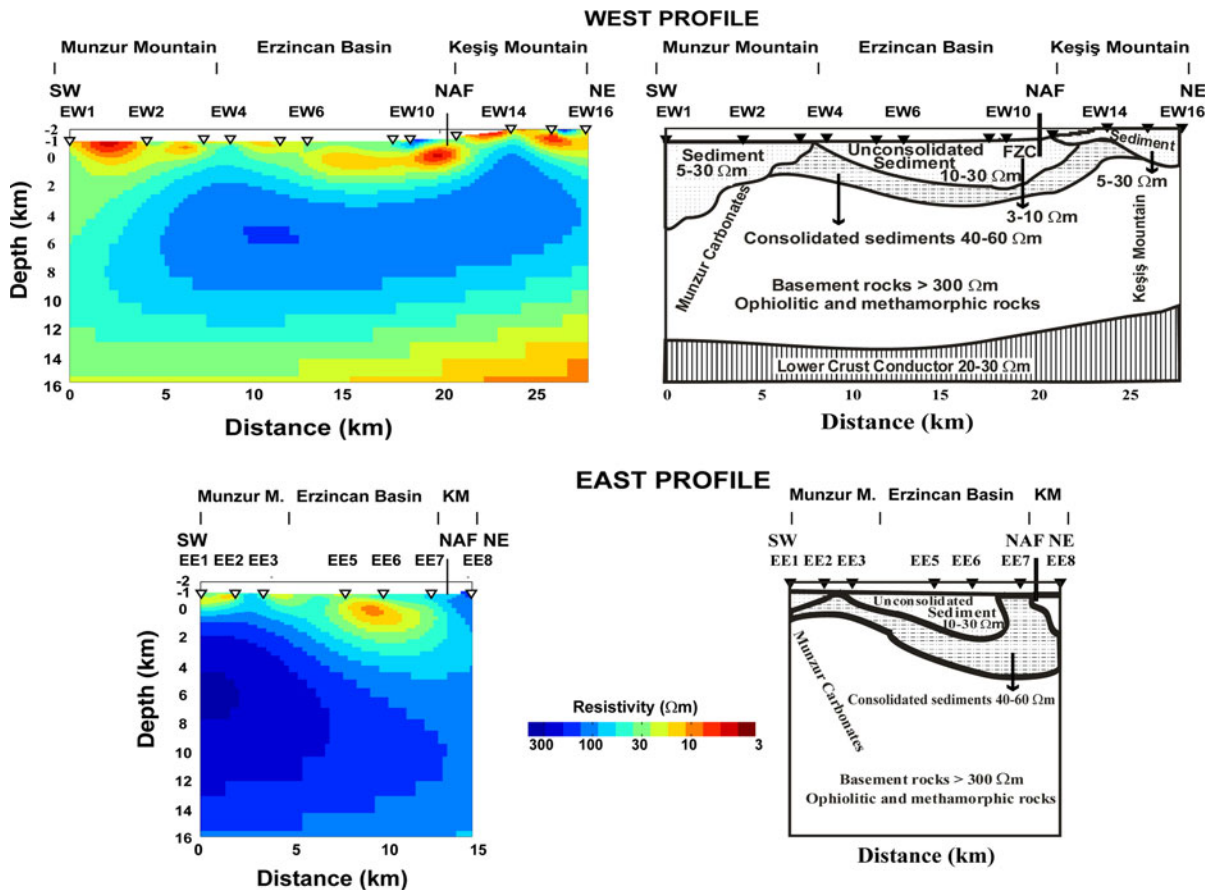
Figure 12
Geological interpretation of the resistivity models of the Erzincan Basin derived from magnetotelluric models

consists of mixed carbonate siliciclastic sedimentary rocks and subordinate volcanogenic rocks.

A high resistivity layer (>300 Ωm) can be observed beneath the Erzincan Basin (Fig. 12) on both profiles, the top of which is at the depth of 4–5 km and represents the crystalline basement rocks (R). Beneath this, a low resistivity layer was imaged at a depth of 14 km in the 2D inversion model of the West Profile (Figs. 10a, 12). The depth of this feature is consistent with the depth of a conductor observed beneath the Anatolian block, bounded by NAF and EAF (TÜRKOGLU et al., 2008).

6.2. Fault Zone Conductor (FZC)

A second conductive zone can be observed in the inversion models (C2). It is located beneath the trace of the NAF and has a resistivity of 3–10 Ωm.

It extends to a depth of 1.5 km in the 2D inversion model of the West Profile, although the stations are sparse, it could be interpreted as a fault zone conductor (FZC). This type of high conductivity zone has been reported from a number of fault zones. The low resistivity could be related to the presence of fluids in interconnected pores or clay minerals in the fault gouge (UNSWORTH et al., 1997; UNSWORTH and BEDROSIAN, 2004; BEDROSIAN et al., 2002, 2004; TANK et al., 2005). The conductive zone C2 is observed in the 3D inversion model for the west profile, but is not observed beneath the NAF on the East profile in the 2D and 3D inversions. This may be due to an inadequate number and coarse spacing of MT stations on the east profile, or perhaps due to differences in the permeability or fluid content of the fault. Note that the sparse station spacing means that this feature is not well defined by the MT data. Continuous

profiling, such as that described by UNSWORTH *et al.* (1997), is needed to give adequate resolution of such features.

6.3. Comparison of Seismic and MT Resistivity Models

Geophysical interpretation has a reduced uncertainty if multiple data sets can be considered. A number of studies have shown that seismic and electrical properties are sometimes correlated and permit a joint analysis (JONES, 1987, 1998; KOZLOVSKAYA and HJELT, 2000; MARQUIS and HYNDMAN, 1992; UNSWORTH *et al.,* 2005).

Figure 13 shows a comparison of seismic velocity and resistivity models for the two profiles in the Erzincan Basin. Sections of P wave velocity (V_p), S wave velocity (V_s) and the ratio of P wave and S wave velocities (V_p/V_s) were obtained from a 3D local earthquake tomography model using aftershocks of the 13 March 1992 Erzincan earthquake (KAYPAK 2008). The seismic model has a nodal spacing of 5 km in the horizontal direction. In the vertical direction the node spacing is 2 km in the upper 10 km and 5 km below that depth (see KAYPAK, 2008 for details). For comparison with the resistivity model, the seismic velocity model was interpolated onto a 0.25 × 0.25 km grid.

The three-dimensional MT inversion model shown in Fig. 10b has a relatively coarse grid. Thus, the two-dimensional MT inversion models were used for joint interpretation (Fig. 13a). Note that the electrical resistivities vary over several orders of magnitude, whereas the seismic velocities vary by just a factor of 3.

6.3.1 Erzincan Basin

Figure 13 shows a clear correlation between the seismic and resistivity models. Both models show the Erzincan Basin as a layer with

- low resistivity (5–30 Ωm)
- low P wave velocity ($V_p < 2$ km/s)
- low S wave velocity ($V_s < 1$ km/s).

Within the Erzincan Basin the low resistivity layer extends to a depth of 3–3.5 km. This agrees with the results of the 1D MT modelling that revealed the basin depth to be 3.25 ± 0.67 km (Fig. 8). Additionally, both the resistivity and the V_p and V_s models clearly indicate the basin becomes deeper towards the northeast. The resistivity sections reveal that the northern edge of the basin has a steeper boundary than the southern side. These results are consistent with the other tomography studies (AKTAR *et al.*, 2004; KAYPAK, 2008). Beneath the Erzincan Basin, the basement rocks are characterised by high resistivity values (>300 Ωm) and high velocities ($V_p > 5.5$ km/s, $V_s > 3$ km/s), which start at a depth of 6 km below sea level.

6.3.2 Internal Structure of the North Anatolian Fault

Both seismic velocity and resistivity models show some evidence for anomalies associated with the North Anatolian Fault. A zone of low resistivity (3–10 Ωm) extends to a depth of 1.5 km below the NAF trace on the West Profile. The low resistivity region below the NAF could be related to aqueous fluids or clay found in the fault gouge on the west section. Typical clays have resistivities in the range 5–20 Ωm (PALACKY, 1987). On the other hand, V_p/V_s values are in the range 1.4–1.7 on both V_p/V_s sections (Fig. 13c). A mean V_p/V_s ratio of 1.81 was estimated from Wadati diagrams for the Erzincan region (KAYPAK and EYIDOĞAN, 2005). The V_p/V_s values observed are relatively low compared to this average value. Fault zones generally consist of fractured shear zones; thus, the elastic properties and electrical conductivities depend on the amount of liquid phase, i.e. porosity, clay content and pore geometry. Generally, high porosity and clay content are associated with a velocity decrease and high V_p/V_s values (HAN *et al.*, 1986; EBERHART-PHILIPS *et al.*, 1995; OLOWOFELA *et al.*, 2004). TAKEI (2002) determined that the presence of aqueous fluids in pores with high aspect ratios will cause low V_p/V_s values. Thus, the low resistivity and low V_p/V_s values could be related to aqueous fluids (KURASHIMO and HIRATA, 2004). Alternatively, low values of V_p/V_s could be related to empty or gas-bearing rocks (KAYPAK, 2008).

On the East Profile, the NAF zone does not exhibit a FZC and the V_p/V_s ratios are low (Fig. 11a, c), which indicates that the pores are empty or not
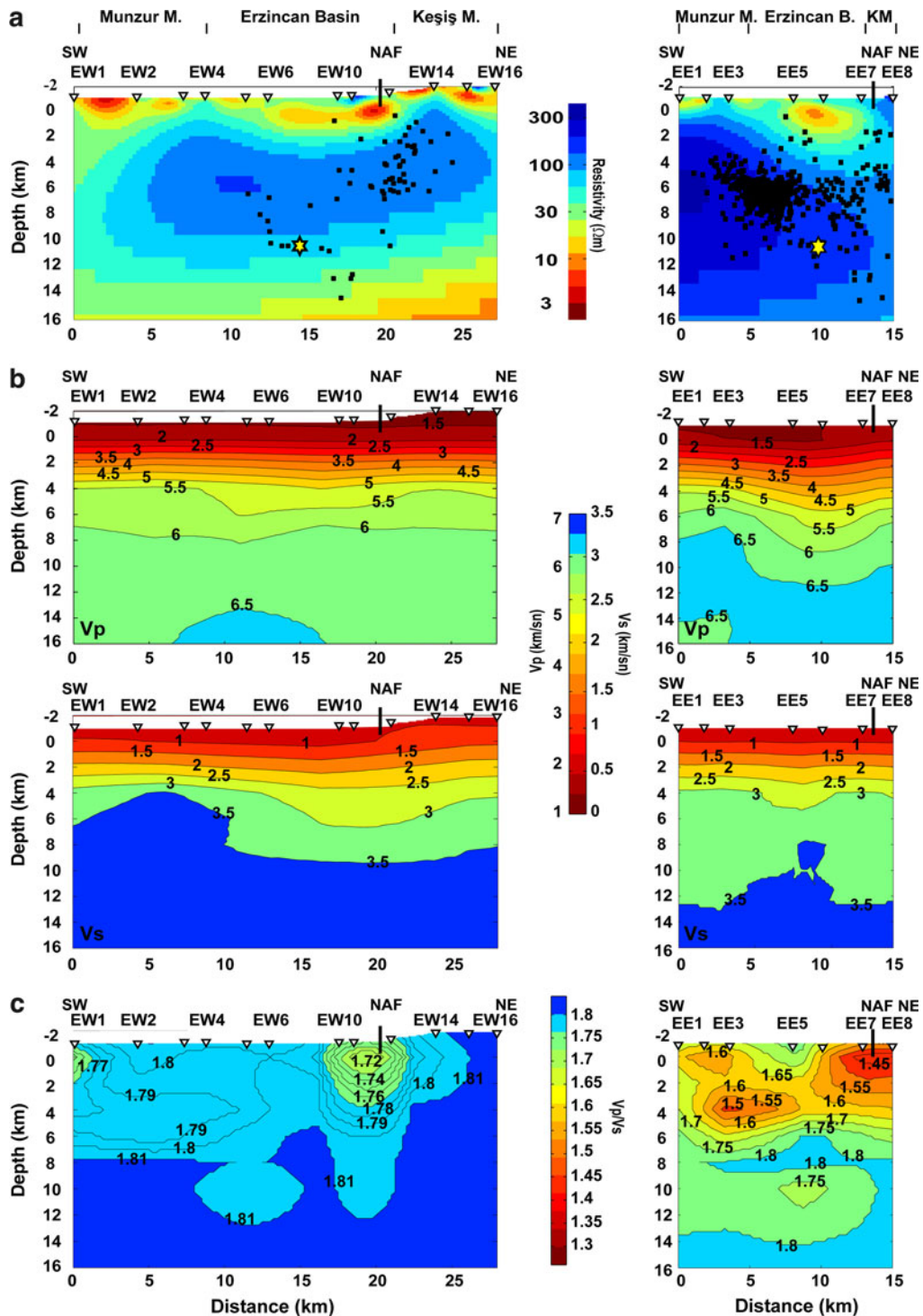
Figure 13

a Electrical resistivity models for the West and East Profiles obtained from 2D inversion of the TE, TM and tipper data. The *star* shows the March 13 1992 earthquake hypocenter, and *black dots* show hypocenters of local events that occurred between 1960 and 2009 projected onto the MT profiles (KOERI and KAYPAK and EYİDOĞAN, 2005). The width of the projection was 20 km. **b** *Vertical depth sections* for V_p anomalies and **c** V_p/V_s anomalies along transects coincident with the resistivity models

interconnected at shallow depths around the fault. This can be interpreted as being due to east-west variations in the permeability of the fault zone or in fluid content.

The relationship between the seismic behaviour of a fault and the resisistivity structure has been examined in many articles (see references in GÜRER and BAYRAK, 2007). To examine the relationship of seismicity and geoelectric structure for the NAF at Erzincan, the earthquakes between 1960 and 2009 and the aftershocks of the 1992 Erzincan earthquake were projected onto the resistivity cross section (Fig. 13a). Most hypocenters occur in the resistive upper crust. This correlation implies that only in the crystalline (resistive) rocks can sufficient stress accumulate for earthquakes to occur (GÜRER and BAYRAK, 2007).

7. Conclusions

The geoelectric structure of the Erzincan Basin was determined using a combination of 1D, 2D and 3D magnetotelluric inversion. The thickness of the unconsolidated sedimentary basin was found to be ~ 3 km. The geometry of the Erzincan Basin was imaged in more detail with the resistivity model than with the seismic velocity model. This is because of the high resistivity contrast between the Erzincan Basin sediments and the underlying crystalline rocks. A FZC may be imaged by the West Profile, but is not observed on the East Profile. This indicates that permeability or fluid availability in the pores of the NAF may vary from west to east at shallow depths.

Acknowledgments

REFERENCES

AKTAR, M., DORBATH, C., and ARPAT, E. (2004), *The seismic velocity and fault structure of the Erzincan Basin, Turkey, using local earthquake tomography,* Geophys. J. Int. *156,* 497–505.

ALLEN, C. R. (1969), *Active faulting in northern Turkey.* Contribution Number 1577, Division of Geology and Science, California Institute of Technology, 32.

AMBRASEYS, N.N. (1970), *Some Characteristic Features of the Anatolian Fault Zone,* Tectonophysics 9, 143–165.

ARPAT, E., and SAROĞLU, F.(1975), *Some Recent Tectonic Events in Turkey,* Bull. Geol. Soc. Turkey *18,* 91–101.

AYDIN, A., and NUR, A. (1982), *Evolution of pull-apart basins and their scale independence,* Tectonics *1,* 91–106.

BAHR, K. (1988), *Interpretation of the magnetotelluric impedance tensor: regional induction and local telluric distortion,* J. Geophys. *62,* 119–127.

BARKA, A.A., TOKSÖZ, M. N., KANDISKY-CADE K., and GÜLEN, L. (1987), *Segmentation, Seismicity and Earthquake Potential of the Eastern Part of the North Anatolian Fault Zone,* Yerbilimeri *14,* 337–352.

BARKA, A., and KANDISKY-CADE, K. (1988), *Strike-slip faulting geometry in Turkey and its influence on earthquake activity,* Tectonics *V7,* 663–684.

BARKA, A., and GÜLEN, L. (1989), *Complex Evolution of the Erzincan Basin (Eastern Turkey) and its Pull-apart and Continental Escape Origin,* J. Struct. Geol. *11,* 275–283.

BARKA, A., and EYIDOĞAN, H. (1993), *The Erzincan earthquake of 13 March 1992 in Eastern Turkey,* Terra Nova *5,* 190–194.

BAYRAK, Y., YILMAZTÜRK, A., and ÖZTÜRK, S. (2005), *Relationship between fundamental seismic hazard parameters for the different source regions in Turkey,* Natural Hazards *36,* 445–462.

BEDROSIAN, P.A., UNSWORTH, M.J., and EGBERT, G. (2002), *Magnetotelluric imaging of the creeping segment of the San Andreas Fault near Hollister,* Geophysical Research Letters *29* (11), 1506.

BEDROSIAN, P.A., UNSWORTH, M.J., EGBERT, G.D., and THURBERD, C.H. (2004), *Geophysical images of the creeping segment of the San Andreas fault: implications for the role of crustal fluids in the earthquake process,* Tectonophysics *385,* 137–158.

BEDROSIAN, P.A., MAERCKLIN, N., WECKMANN, U., BARTOV, Y., RYBERGI T., and RITTER, O. (2007), *Lithology-derived structure classification from the joint interpretation of magnetotelluric and seismic models,* Geophys. J. Int. *170,* 737–748.

BERDICHEVSKY, M.N., DIMITRIEV, V.I., POZDNJAKOVA, E.E. (1998), *On two dimensional interpretation of magnetotelluric soundings*, Geophys. J. Int. *133*, 585–606.

BERNARD, P., GARIEL, J., and DORBATH, L. (1992), *Fault Location and Rupture Kinematics of the Magnitude 6.8, 1992 Erzincan earthquake, Turkey, from strong ground motion and regional records*, Bull. of Seis. Society of America *V87*, No-5, 1230–1243.

BIBBY, H.M., CALDWELL, T.G., and BROWN, C. (2005), *Determinable and non-determinable parameters of galvanic distortion in Magnetotellurics*, Geophys. J. Int. *163*, 915–930.

BOERNER, D.E., KURTZ, R.D., CRAVEN, J.A., RONDENAY, S., and QIAN, W. (1995), *Buried Proterozoic foredeep under the Western Canada Sedimentary Basin?* Geology April v.*23*, no. 4, 297–300.

BOOKER, J.R., FAVETTO, A., and POMPOSIELLO, M.C. (2004), *Low electrical resistivity associated with plunging of the Nazca flat slab beneath Argentina*, Nature *429*, 399–403.

CALDWELL, T.G., BIBBY, H.M., and BROWN, C. (2004), *The magnetotelluric phase tensor*, Geophys. J. Int. *158*, 457–469.

DEWEY, J.F., and ŞENGÖR, A.M.C. (1979), *Aegean and surrounding regions: Complex multi plate and continuum tectonics in a convergent zone*, Geol. Soc. of Am. Bull. part.1, v.*90*, 84–92.

EBERHART-PHILIPS, D., STANLEY, W.D., RODRIGUEZ, B.D., and LUTTER, W.J. (1995), *Surface seismic and electrical methods to detect fluids related to faulting*. Journal of Geophysical Research Vol. *100*, No. B7, 12, 919–1293.

EGBERT, G.D. (1997), *Robust multiple-station magnetotelluric data processing*. Geophys. J. Int. *130*, 475–496.

EGBERT, G.D., and BOOKER, J.R. (1986), *Robust estimation of geomagnetic transfer functions*, Geophys. J.R. Astron. Soc. *87*, 173–194.

ERDIK, M., YÜZÜGÜLLÜ, O., YILMAZ, C., and AKKAS, N. (1992), 13 March (Ms = 6.8) *Erzincan Earthquake: A preliminary reconnaissance report*, Soil Dynam. Earthq. Enging.*11*, 279–310.

FUENZALIDA, H., DORBATH, L., CISTERNAS, A., EYIDOĞAN, H., BARKA, A., RIVERA, L., HAESSLER, H., and LYBERIS, N. (1997), *Mechanism of the 1992 Erzincan earthquake and its aftershocks, tectonics of the Erzincan basin and decoupling on the North Anatolian Fault*. Geophys. J. Int., *129*, 1–28.

GAUCHER, E. (1994), *Modele en porofondeur et en vitessedu basin d'Erzincan D.E. A*. Institut de Physique Globe de Paris.

GAMBLE, T.D., GOUBAU, W.M., and CLARKE, J. (1979), *Magnetotellurics with a remote reference*, Geophysics *44*, 53–68,

GÖKALP, H. (2007), *Local earthquake tomography of the Erzincan basin and surrounding area in Turkey*, Annals of Geophysics Vol *50*. N.6.

GROOM, R. W., and BAILEY, R. C. (1989), *Decomposition of magnetotelluric impedance tensors in the presence of local three-dimensional galvanic distortion*, Journal of Geophysical Research *94*, 1913–1925.

GROSSER, H., BAUMBACH, M., BERCKHEMER, H., BAIER, B., KARAHAN, A., SCHELLE, H., KRÜGER, F., PAULAT, A., MICHEL, G., DEMIRTAŞ, R., GENCOĞLU, S., and YILMAZ, R. (1998), *The Erzincan (Turkey) earthquake (Ms = 6.8) of March 13, 1992 and its aftershock sequence*, PAGEOPH Vol. *152*, 465–505.

GÜNDOĞDU, O., ALTINOK, Y., HISARLI, M., and BEYAZ, H. (1992), 13 Mart 1992 Erzincan depremi gözlem değerlendirmeleri, Erzincan Depremi ve Türkiye Deprem Sorunu, ITU, Maden Fakültesi Yayını, 56–62.

GÜRBÜZ, A. (2010), *Geometric characteristics of pull-apart basins*, Lithosphere v.*2*, no.3, 199–206.

GÜRER, A., and BAYRAK, M. (2007), *Relation between electrical resistivity and earthquake generation in the crust of West Anatolia, Turkey*, Tectonophysics *445*, 49–65.

HAN, DE-HUA., NUR, A., and MORQAN, D. (1986), *Effects of porosity and clay content on wave velocities in sandstones*, Geophysics Vol. *51*. No. 11, P. 2093·2107,13.

HANSEN, P.C. (1992), *Analysis of discrete ill-posed problems by means of the L-curve*,Society for Industrial and Applied Mathematics *34*, 561–580.

HARTLEB, R.D., DOLAN, J.F., KOZACI, Ö., AKYÜZ, S., and SEITZ, G.G. (2006), *A 2500-yr- long paleoseismological record of large, infrequent earthquakes on the North Anatolian Fault at Çukurçimen, Turkey*, GSA Bulletin v.*118*, no. 7/8, p.823–840.

HEMPTON, M.R., and DUNNE, L.A. (1984), *Sedimentation in Pull-apart Basins: Active Examples in Eastern Turkey*, J. Geol. *92*, 513–530.

JONES, A.G. (1998), *Waves of the future: Superior inferences from collocated seismic and electromagnetic experiments*, Tectonophysics *286*, 273–298.

JONES, A.G. (1987), *MT and reflection: an essential combination*, Geophys. J. R. astr. Soc., *89*, 7–18.

KARSLI, O., CHEN, B., UYSAL, I., AYDIN, F., WIJBRANS, J.R., and KANDEMIR, R. (2008), *Elemental and Sr–Nd–Pb isotopic geochemistry of the most recent Quaternary volcanism in the Erzincan Basin, Eastern Turkey: framework for the evaluation of basalt–lower crust interaction*, Lithos *106*, 55–70.

KAYPAK, B., and EYIDOĞAN, H. (2005), *One-dimensional crustal structure of the Erzincan basin, Eastern Turkey and relocations of the 1992 Erzincan earthquake (Ms = 6.8) aftershock sequence*, Physics of the Earth Planetary Interiors *151*, 1–20.

KAYPAK, B. (2008), *Three dimensional V_p and V_p/V_s structure of the upper crust in the Erzincan basin eastern (Turkey)*, Journal of Geophysical Research v113, B07307.

KELLER, G.V., *Rock and mineral properties*, Electromagnetic methods in applied geophysics theory: (ed., Nabighian, M.N.) (Tulsa, Okla., Society of Exploration Geophysicists, 1987) v. 1, p. 13–51.

KOÇYIĞIT, A. (2003), *Two-stage Evolutionary Model for the Erzincan Pull-Apart Basin on the North Anatolian Fault System (NAFS)*, "International Workshop on the North Anatolian, East Anatolian and Dead Sea Fault System:Recent Prog.", p.31.

KOZLOVSKAYA, E., HJELT, S.E. (2000), *Modeling of Elastic and Electrical Properties of Solid-Liquid Rock System with Fractal Microstructure*. Phys. Chem.Earth, Vol.*25*, No.2, 195–200.

KURASHIMO, E., and HIRATA, N. (2004), *Low Vp and Vp/Vs zone beneath the northern Fossa Magna basin, central Japan, derived from a dense array observation*, Earth Planets Space *56*, 1301–1308, 2004.

MACKIE, R. L., and MADDEN, T. R. (1993), *Three-dimensional magnetotelluric inversion usingconjugate gradients*, Geophys. J. Int. *115*, 215–229.

MARQUIS G., and HYNDMAN D.R. (1992), *Geophysical support for aqueous fluids in the deep crust: seismic and electrical relationships*, Geophys. J. Int. *110*, 91–105.

MCCLUSKY, S., BALASSANIAN, S., BARKA, A., DEMIR, C., ERGINTAV, S., GEORGIEV, I., GURKAN, O., HAMBURGER, M., HURST, K., KAHLE, H., KASTENS, K., KEKELIDZE, G., KING, R., KOTZEV, V., LENK, O., MAHMOUD, S., MISHIN, A., NADARIYA, M., OUZOUNIS, A., PARADISSIS, S., PETER, Y., PRILEPIN, M., REILINGER, R., SANLI, I., SEEGER, H., TEALEB, A., TOKSOZ, M., and VEIS, G. (2000), *GPS constraints on plate motion and deformation in the eastern Mediterranean:*

Implications for plate dynamics, Journal of Geophysical Research 105, 5695–5719.

MCKENZIE, D.P. (1972), *Active Tectonics of the Mediterranean Region*, Geophs. Jour.Royal.Astron.Soc. *30*, 109–185.

MCNEICE, G.M., and JONES, A.G. (2001), *Multisite, multifrequency tensor decomposition of magnetotelluric data*, Geophysics *66*, 158–173.

MEJU, M.A., GALLARDO, L.A., MOHAMED, A.K. (2003), *Evidence for correlation of electrical resistivity and seismic velocity in heterogeneous near-surface materials* Geophysical Research Letters, Vol. 30, No. 7, 1373.

OLOWOFELA, J.A., KAMIYOLE I, C., and ADEGOKE, J.A. (2004), *Effects of Clay content and porosity on wave velocities in unconsolidated Media using Empirical relations*, J. Geophys.Eng. *I*, 234–239.

OLSEN, K.B., ARCHUELETA, R.J., and MATARESE, J.R. (1995), *Three dimensional simulation of a magnitude 7.75 earthquake on the San Andreas fault*, Science *270*, 1628–1632.

OLSEN, K.B. (2000), *Site amplification in Los Angeles basin from three dimensional modelling of ground motion*, Bulletin of seismological society of America, *90* 6B, 77–94.

OVER, S., K. S. KAVAK, O. BELLIER, and S. OZDEN, *Is the Amik Basin (SETurkey) a Triple Junction Area? Analyses of SPOT XS Imagery and Seismicity*, Int. J. Remote Sensing, **25/19**, 3857–3872, 2004.

ÖZGÜL, N., and TURŞUCU, A. (1984), *Stratigraphy of the Mesozoic carbonate sequence of the Munzur Mountains (eastern Taurides)*, in Geology of the Taurus Belt, (eds.) Tekeli, O, and Göncüoğlu, M., General Directorate and Mineral Research and Exploration, Ankara, pp 173–180.

PADILHA, A.L., VITORELLO, I., and BRITO M.P.A. (2002), *Magnetotelluric soundings across the Taubat′e Basin, Southeast Brazil.* Earth Planets Space *54*, 617–627.

PALACKY, G.J. (1987), Resistivity characteristics of geologic targets, *in* Nabighian, M.N., ed., E*lectromagnetic methods in applied geophysics: Tulsa, Okla.*, Society of Exploration Geophysicists v.*1*, p. 53–129.

PARKINSON, W. D. (1962), *The influence of continents and oceans on geomagnetic variations*, Geophysical Journal of the Royal Astronomical Society 6, 441–449.

POMPOSIELLO, M.C., FAVETTO, A., SAINATO C., BOOKER, J., and SHENGHUI, L. (2002), *Imaging the sedimentary basin of the Tucuman Plain in the northern Pampean Ranges, Argentina*, Journal of Applied Geophysics *49*, 47–58.

REILINGER, R., 25 others., (2006), *GPS constraints on continental deformation in the Africa-Arabia-Eurasia continental collision zone and implications for the dynamics of plate interactions*, Journal of Geophysical Research Vol*111*, B05411.

RICE, S.P., ROBERTSON, A. H. F., USTAÖMER, T., İNAN, N., and TAŞLI, K. (2009), *Late Cretaceous –Early Eocene tectonic development of the Tethyan suture zone in the Erzincan area, Eastern Pontides, Turkey.* Geol. Mag. *146* (4), 567–590.

RODI, W., and MACKIE, R.L. (2001), *Nonlinear conjugate gradients algorithm for 2-D magnetotelluric inversion*, Geophysics *66*, 174–187.

SASAKI, Y. (2001), *Full 3-D Inversion of electromagnetic data on PC*, J. Appl. Geophys., *46*, 45–54.

SIRIPUNVARAPORN, W., EGBERT, G., LENBURY, Y., and UYESHIMA, M. (2005), *Three-dimensional magnetotelluric inversion: data-space method, Physics of the Earth and Planetary Interiors 150*, 3–14.

STEIN, S., BARKA, A.A., and DIETERICH H.J. (1997), *Progressive failure on the North Anatolian fault since 1939 by earthquake stress triggering*, Geophys. J. Int. Vol. *128*, Issue 3, pages 594–604.

ŞENGÖR, A.M.C. (1979), *The North Anatolian transform fault: its age, offset and tectonic significance*, J. Geol. Soc., London *136*, 269–282.

ŞENGÖR, A. M. C., TÜYSÜZ, O., İMREN, C., SAKıNC, M., EYIDOĞAN, H., GÖRÜR, N., LE PICHON, X., and RANGIN C. (2005), *The North Anatolian Fault: A new look*, Annu. Rev. Earth Planet. Sci. *33*, 37–112.

TAKEI, Y.(2002), Effect of pore geometry on *Vp/Vs*: *From equilibrium geometryto crack*, *J.* Geophys. Res. *107*(B2), 2043. doi: 10.129/2001JB000522.

TANK, S.B., HONKURA, Y., OGAWA, Y., MATSUSHIMA, M., OSHIMAN, N., TUNCER, M.K., CELIK, C., TOLAK, E., and ISIKARA, A.M. (2005), *Magnetotelluric imaging of the fault rupture area of the 1999 Izmit (Turkey) earthquake*, Physics of the Earth and Planetary Interiors *150*, 213–225.

TATAR, Y. (1978), *Tectonic Study of the Erzincan-Refahiye Section of the North Anatolian Fault Zone*, Hacettepe Univ. Earth Sci. 4, 201–236.

TIKHONOV, A.N., and ARSENIN, V.Y. (1977), *Solutions of Ill-Posed Problems*, V.H. Winston and Sons: Washington, D.C.

TÜRKOGLU, E., UNSWORTH, M., ÇAGLAR, İ., TUNCER, V., and AVŞAR, Ü. (2008), *Lithospheric structure of the Arabia-Eurasia collision zone in eastern Anatolia: Magnetotelluric evidence for widespread weaking by fluids?* Geology 36, 619–622.

TÜRKOĞLU, E. (2009), *A Magnetotelluric Investigation of the Arabia–Eurasia Collision in Eastern Anatolia*, University of Alberta, Phd thesis, pp-208.

TÜYSÜZ, O. (1993), *Erzincan çevresinin jeolojisi ve tektonik evrimi, 2. Ulusal Deprem Mühendisliği Konferansı.* 10–13, Mart, Istanbul.

UNSWORTH, M.J., MALIN, P., EGBERT, G.D., and BOOKER, J.R. (1997), *Internal structure of the San Andreas fault at Parkfield, California,* Geology 25, 359–362.

UNSWORTH, M.J., and BEDROSIAN, P.A. (2004), *Electrical resistivity at the SAFOD site from magnetotelluric exploration*, Geophys. Res. Lett. *31*, L12S05.

UNSWORTH, M.J., JONES A.G., WEI, W., MARQUIS, G., GOKARN, G.S., SPRATT J.E., and the INDEPTH-MT team. (2005), *Crustal rheology of the Himalaya and Southern Tibet inferred from magnetotelluric data*, Nature Vol*43*,8|3.

WANNAMAKER, P.E., BOOKER, J.R., JONES, A.G., CHAVE, A.D., FILLOUX, J.H., WAFF, H.S., and LAW, L.K. (1989), *Resistivity cross section through the Juan deFuca subduction system and its tectonic implications*, J. Geophys. Res. *94*, 14127–14144.

WESTAWAY R., and ARGER, J. (2001), *Kinematics of the Malatya–Ovacık Fault Zone*, Geodinamica Acta *14*, 103–131.

WIESE, H. (1962), *Geomagnetische tiefentellurik*, Pure and Applied Geophysics *57*, 31–46.